# Stacking of Hexagonal Nanocrystal Layers during Langmuir–Blodgett Deposition

Detlef-M. Smilgies,*,[†] Andrew T. Heitsch,[‡] and Brian A. Korgel[‡]

[†]Cornell High Energy Synchrotron Source (CHESS), Cornell University, Ithaca New York 14853, United States
[‡]Department of Chemical Engineering, Texas Materials Institute, Center for Nano- and Molecular Science and Technology, The University of Texas at Austin, Austin, Texas 78712-1062, United States

**ABSTRACT:** Hexagonally ordered close-packed monolayers of sterically stabilized FePt nanocrystals were deposited on substrates using the Langmuir–Blodgett technique. Monolayers of nanocrystals were also stacked by sequential Langmuir–Blodgett transfer. The structures of the nanocrystal monolayers and multilayer stacks were examined with scanning electron microscopy (SEM) and grazing-incidence small-angle scattering (GISAXS). An analytical model derived from the quasikinematic approximation provides a convenient description of the GISAXS data of the stacked layers. The transferred monolayers showed good in-plane hexagonal order, even for trilayers. Bilayers exhibited spatial registry with the top layer positioned above the 3-fold coordinated sites of the bottom layer. Trilayers, on the other hand, exhibited significant disorder.
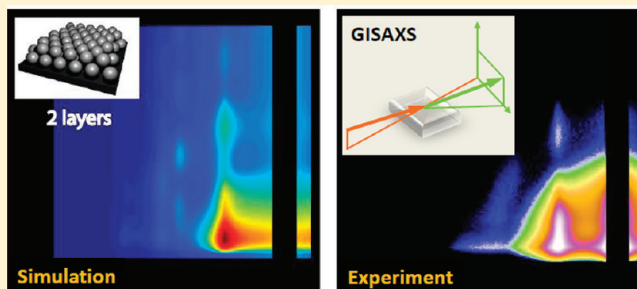
## INTRODUCTION

The advent of methods for nanocrystal synthesis that produce particles with well-controlled size, shape, and ligand shells has enabled the formation of synthetic metamaterials of ordered nanocrystal assemblies.[1−4] The properties of these nanocrystal superlattices derive from the unique size-dependent properties of the nanocrystals combined with interparticle electronic coupling between neighboring nanocrystals arranged on a regular lattice, analogous to atom- and molecule-based solid state materials.

Nanocrystals can be deposited onto flat surfaces such as silicon wafers or glass slides with excellent order and orientation by simple solvent evaporation from a nanocrystal dispersion by fine-tuning the drop casting parameters.[5] However, thicker nanocrystal deposits covering large substrate areas are typically rough with extensive cracking.[6] Various other deposition methods can produce much more extended and uniform superlattice films, such as Langmuir–Blodgett (LB) deposition,[7−15] convective self-assembly,[16] inclined plane deposition,[17−19] and hot doctor blading.[20]

Due to the size of the nanocrystals (ranging approximately from of 2−20 nm), the structural characterization of these superlattices falls in the realm of small-angle X-ray scattering (SAXS). A convenient technique to characterize nanocrystals superlattices in situ and in real-time is synchrotron-based grazing-incidence small-angle X-ray scattering (GISAXS).[6,21−23] GISAXS provides highly precise and proper statistically averaged information about two- (2D) and three-dimensional (3D) superlattices. In addition, GISAXS is compatible with in situ experiments such as solvent vapor annealing[6] and casting

from solution,[16] and provides real-time information about how nanocrystals assemble and order.

Well-ordered nanocrystal superlattices can enable detailed studies of collective nanocrystal behavior[1−4,13,24] and are important building blocks in the field of nanostructured artificial solids.[1−4] LB deposition has been established as a route to deposit nanocrystal monolayers covering extensive substrate areas. But it is not known whether sequential stacking of LB monolayers (see Figure 1) can yield spatial registry between stacked planes. Here we find that bilayers exhibit spatial registry, but the stacking of additional layers leads to out-of-plane disorder.

## EXPERIMENTAL SECTION

**a. Synthesis.** FePt nanocrystals were synthesized by solvent-based arrested precipitation using a modification of a previously published procedure.[25] Typical reactions yield approximately 150 mg of Fe−Pt nanocrystals coated by ligands oleylamine and oleic acid with an average composition of $Fe_{0.42}Pt_{0.58}$ measured by energy dispersive spectroscopy (EDS) and an average core diameter of 6.9 nm.[13,14] Purified Fe−Pt nanocrystals were stored as 10 mg/mL dispersions in chloroform. Silicon substrates of 1.0 cm$^2$ area were cleaned by sequential immersion in chloroform, acetone, and then isopropanol with mild sonication for 2 min. The substrates were dried with compressed air between each cleaning step.
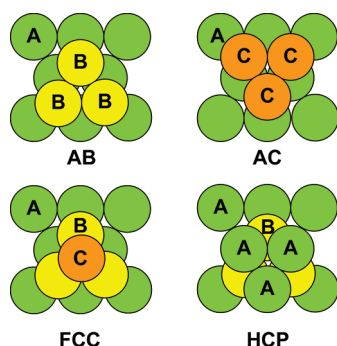
**Figure 1.** FCC and HCP stacking for a finite number of layers. For two layers there are two possible positions B and C (top row) that give rise to identical scattering. For 3 layers and more (bottom row) there is either FCC (ABCABC...) or HCP stacking (ABABAB...), and scattering patterns are distinguishable.

**b. Deposition.** Nanocrystal films were transferred to Si substrates using the LB technique.[13,14] Substrates were fully submerged prior to spreading the nanocrystals on the aqueous subphase. After the nanocrystals were spread dropwise onto the water surface and compressed to a desired surface pressure of 47.0 mN/m, the Si substrate was immediately withdrawn normal to the water surface at a rate of 1.0 mm/min. This procedure deposited one monolayer of nanocrystals onto the Si substrate. The process was repeated to form stacks of two and three monolayers on the Si substrates.

**c. Characterization.** After preparation, LB films were imaged with a Zeiss Supra 40 scanning electron microscope (SEM) at a 5−7 mm working distance and a 10 kV working voltage.

GISAXS measurements were performed at the D1 beamline of the Cornell High Energy Synchrotron Source (CHESS). D1 is supplied with a high-flux X-ray beam from a Mo:B$_4$C multilayer monochromator providing $10^{12}$ photon/s mm$^2$ at 10 keV photon energy with a bandwidth of 1.5%. The incident beam was collimated with two slits of 0.5 mm horizontal (H) gap and 0.1 mm vertical (V) gap, about 1 m apart. Parasitic scatter was removed by a guard slit (0.7 mm H, 0.2 mm V) about 0.5 m downstream from the second collimation slit. Samples were mounted on a 4-axis goniometer controlling incident angle and parasitic tilt, as well as sample height and lateral position. Scattered X-ray photons were detected with a MedOptics CCD camera at a sample-to-detector distance of 673 mm. The area detector was protected from the intense scattering of the direct beam as well as the specular and diffuse reflected radiation with a 3 mm diameter tantalum rod as a beamstop. The detector was calibrated using a direct beam image (obtained with attenuation) and a silver behenate standard. Samples and beamstop were lined up in the direct beam using an ion chamber. After line-up, the ion chamber was removed, and images could be acquired at various incident angles and lateral positions on the sample.

## ■ SCATTERING THEORY FOR ORDERED NANOCRYSTAL LAYERS

GISAXS is a convenient scattering technique to characterize nanostructured thin films; however, the full scattering theory within the framework of distorted wave Born approximation is complex.[26−28] In certain cases, the scattering theory can be simplified. For scattering from nanocrystal layers, the quasi-kinematic approximation[14,29] is applicable, since (i) the

nanocrystal layers are thin, and (ii) an incident angle sufficiently above the substrate critical angle is used. At an incident angle of $\alpha_i = 0.25°$ versus a substrate critical angle $\alpha_c = 0.18°$ at 10 keV photon energy, the reflected beam intensity is less than a tenth of the incident beam intensity, and the wave field of the reflected beam can be neglected. In addition, scattering angles are large enough compared to the critical angle so that refraction effects can be ignored.

Within the quasi-kinematic approximation, scattering intensities can be split into contributions of the form factor of the individual nanocrystals and the structure factor of the nanocrystal assembly, as is commonly done for transmission small-angle scattering applying the local monodisperse approximation.[30] For GISAXS, surface scattering features have to be included such as scattering rods and the Vineyard peak.[31,32] The description is straightforward within the quasi-kinematic approach for a monolayer;[14] however, additional complications arise for modeling a finite, well-specified number of layers, as detailed below.

Scattering intensities are conveniently expressed as a function of the scattering vector **q**. The modulus of **q** is $q = 4\pi \sin(2\theta/2)/\lambda$, where $\lambda$ is the X-ray wavelength and $2\theta$ is the scattering angle. For grazing incidence diffraction, it is convenient to separate **q** into a parallel component $q_\parallel$ and a perpendicular component $q_\perp$ with respect to the sample surface. If intensity is detected at a point $(x,z)$ on the area detector, this corresponds to scattering angles $\mu$ in the horizontal plane and $\nu$ in the vertical plane,

$$\tan(\mu) = x/L$$

$$\tan(\nu) = z/\sqrt{L^2 + x^2} \tag{1}$$

assuming that the area detector is arranged perpendicular to the incident X-ray beam and that the direct X-ray beam strikes the detector in the point $(0,0)$ at a distance $L$ from the sample. In the small-angle approximation, the wave vector components can be expressed as

$$q_\parallel = 2\pi \sin(\mu)/\lambda$$

$$q_\perp = 2\pi \sin(\nu)/\lambda$$

$$q = \sqrt{q_\parallel^2 + q_\perp^2} \tag{2}$$

The last line of eq 2 relates the wave vector modulus to its parallel and perpendicular components.

**a. Form factor.** Transmission electron microscopy (TEM) images showed that FePt nanoparticles are essentially spherical in shape. The spherical form factor is given by[30]

$$F(q) = \left| \frac{4}{3}\pi R^3 \left( 3\frac{\sin(qR) - qR\cos(qR)}{(qR)^3} \right) \right|^2 \tag{3}$$

The size distribution $P(R)$ of the particles, as confirmed by TEM, is typically Gaussian in shape, with a standard deviation $\sigma$ from the mean radius $R_0$:

$$P(R) = \frac{1}{\sqrt{2\pi}\,\sigma} \exp\left( -\frac{(R - R_0)^2}{2\sigma^2} \right) \tag{4}$$

The organic ligand coating on the nanocrystals does not contribute significantly to the X-ray scattering intensity, and thus $P(R)$ provides a measure of the inorganic core size. The
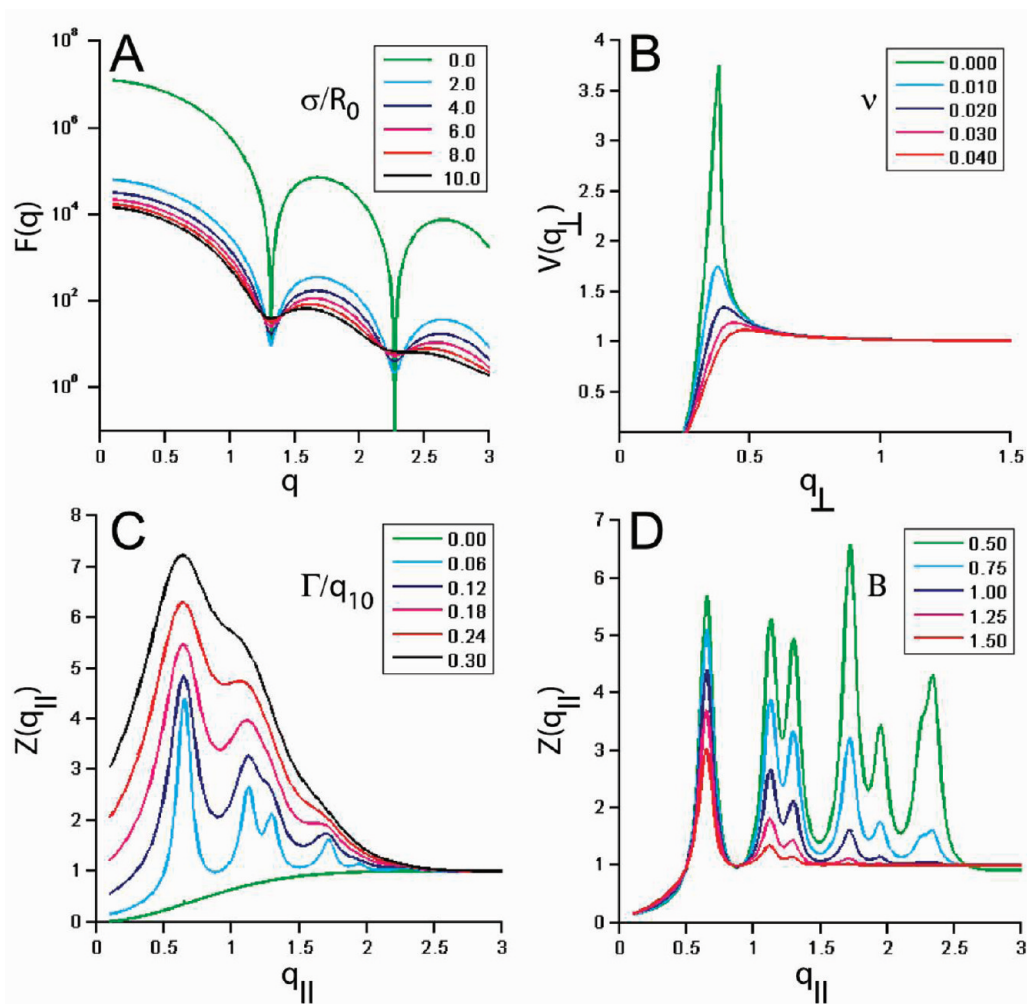
**Figure 2.** Basic ingredients of the nanocrystal layer model: (A) form factor, (B) Vinyard factor, and (C,D) structure factor. Shown is the dependency of these contributions on the essential parameters: (A) polydispersity $\sigma/R_0$, (B) effective X-ray absorption at the interface $v$, (C) grain size via relative peak width $\Gamma/q_{10}$, and (D) static disorder parameter $B$. For details see text.

size distribution of the cores influences the scattering signal, and the averaged form factor can be written as

$$\bar{F}(R) = \int P(R)F(R)\, dR \qquad (5)$$

The degree of polydispersity is then given as $\sigma/R_0$. The form factor of the nanocrystals can be precisely characterized by SAXS from a dilute dispersion.

**b. Structure Factor.** A monolayer of spherical particles forms a closely packed hexagonal layer. Each hexagonal domain is of finite size, and when deposited on an unstructured surface such as the amorphous surface oxide of a silicon wafer, these grains have random orientation laterally. Because the grazing-incidence X-ray beam illuminates a macroscopic strip of sample (typically 10−20 mm long ×0.5 mm wide), a 2D powder pattern results, which is given by the multiplicities $m_{hk}$ and lineshapes $L(q_x − q_{hk}, w_{hk})$ of the reflections. A finite-size grain model for the monolayer structure factor $Z_0(q_x)$ can be obtained by associating each reflection $q_{hk}$ with a finite width $w_{hk}$, as given by the Scherrer formula:[33]

$$Z_0(q_\parallel) = \sum_{hk} m_{hk} L(q_\parallel − q_{hk}, w_{hk}) \qquad (6)$$

Typically, Gaussian or Lorentzian lineshapes are used.[30] For an average domain size of $D$, the associated Lorentzian distribution function is given by

$$L(q_\parallel − q_{hk}, \Gamma) = \frac{1}{1 + \left(\frac{q_\parallel − q_{hk}}{\Gamma}\right)^2} \qquad (7)$$

and the full width at half-maximum $2\Gamma$ is related to the average domain size $D$ by

$$2\Gamma = \frac{2\pi K}{D} \qquad (8)$$

with $K \approx 0.9$ being the Scherrer constant.[33]

All in-plane reflections with identical $q_{hk} = \|\mathbf{q}_{hk}\|$ lie on the same powder ring. For a close-packed hexagonal layer, the q-vectors follow the simple series

$$q_{hk}/q_{10} = \sqrt{h^2 + hk + k^2} \qquad (9)$$

and $q_{10}$ is given by the hexagonal lattice constant $a$ as $q_{10} = 2\pi\sqrt{3}/2a$.

In soft matter systems, disorder plays an important role. Disorder of the first kind—in which the lattice retains long-
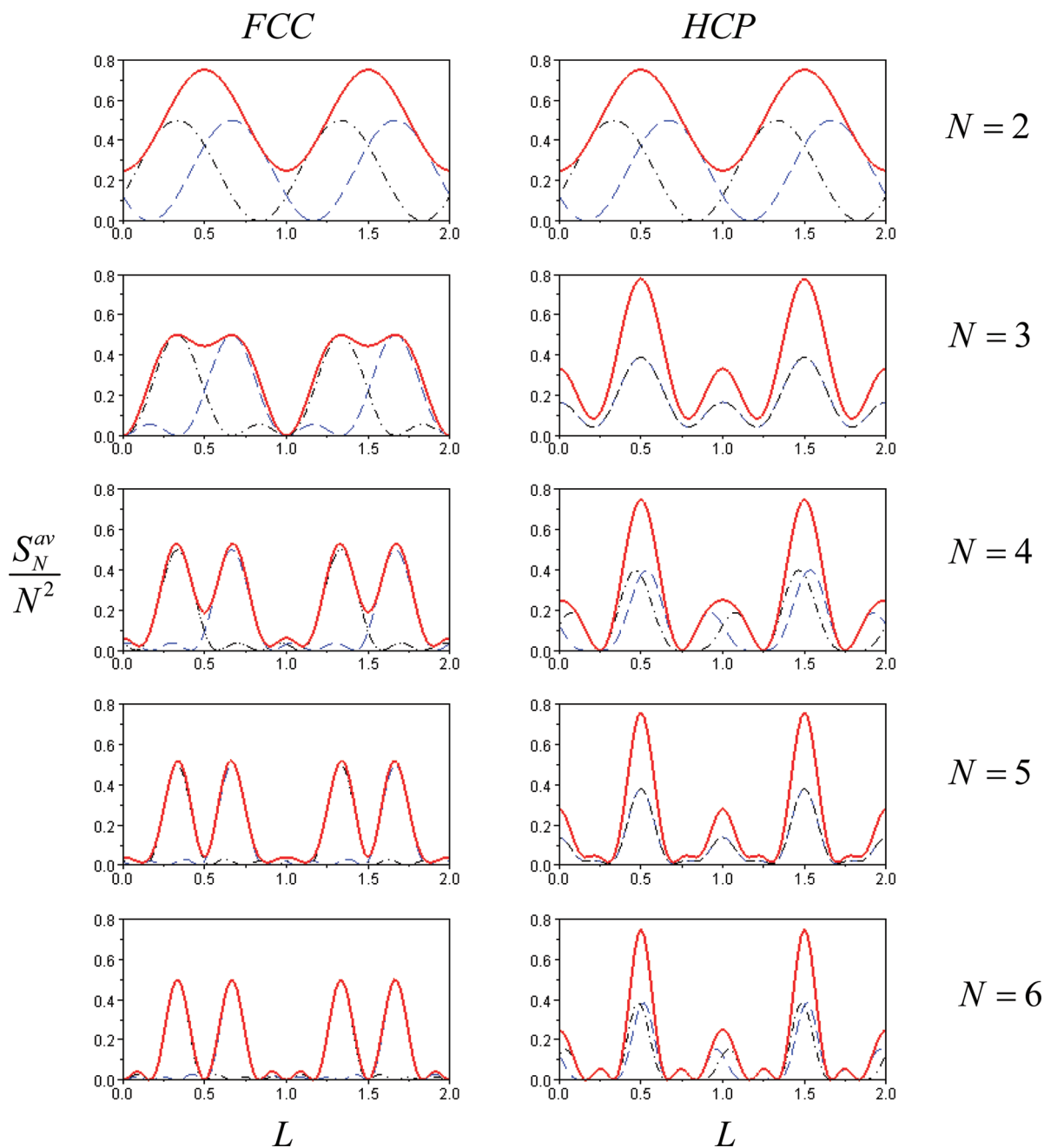
**Figure 3.** Calculated layer structure factors normalized by $N^2$ along the first-order rods ($10L$) and ($01L$) for finite layer systems ($N = 2-6$) with FCC (left column) and HCP stacking (right column). The perpendicular wave vector component is related to the continuous index $L$ via $q_\perp = 2\pi L/c$. Contributions from individual rods (blue dashed line for ($10$) and black dash-dotted line for ($01$)) as well as their powder average (red solid line) are plotted. Note that the bilayer system is degenerate. HCP and FCC packing sequences become distinguishable with the addition of a third layer.

range order—can be modeled by introducing a static Debye–Waller factor $W$:[30]

$$Z(q_\parallel) = Z_0(q_\parallel)W(q_\parallel) + (1 - W(q_\parallel)) \tag{10}$$

with

$$W(q_\parallel) = \exp(-B^2 q_\parallel^2) \tag{11}$$

**c. Surface Scattering.** For a few nanocrystal layers on a surface, the surface scattering away from the incident plane can be described by Vinyard theory.[26,29,31] The dynamic scattering effects give rise to the Vinyard function

$$\tilde{V}(k_{i\perp}, k_{f\perp}) = \left| \frac{2k_{f\perp}}{k_{f\perp} + \sqrt{k_{f\perp}^2 - k_c^2}} \right|^2 \tag{12}$$

where $k_{i\perp}$ and $k_{f\perp}$ are the normal components of the wave vectors of the incoming and scattered X-ray beams, and $k_c = (2\pi/\lambda)\sin(\alpha_c)$ is the critical wave vector as given by the X-ray wavelength $\lambda$ and the critical angle $\alpha_c$ of the substrate.[32] If $k_{f\perp}$ goes negative, the X-ray exit angle lies below the sample horizon, and due to X-ray absorption, none of these X-ray beams can reach the detector. Hence we set $V = 0$ in this case.

We observe that $k_{f\perp}$ is related to the perpendicular component of the scattering vector

$$q_\perp = k_{f\perp} - k_{i\perp} \tag{13}$$

In our chosen scattering geometry, the incident angle is fixed at $\alpha_i = 0.25°$ and slightly above the substrate critical angle of $0.18°$. Thus $k_{i\perp}$ is a constant given by

$$k_{i\perp} = -(2\pi/\lambda)\sin(\alpha_i) \tag{14}$$

and we can rewrite the Vinyard factor as a function of $q_\perp$:

$$V(q_\perp) = \tilde{V}(k_{i\perp}, q_\perp + k_{i\perp}) \tag{15}$$

The above Vinyard factor holds for the case of no absorption at the interface. However, nanoparticle cores often feature atoms with a high number of electrons, for instance Au or PbS nanocrystals. This leads to absorption at the interface, which reduces the Vinyard enhancement. Rather than developing a complex multicomponent scattering theory,[28,34] we found that by including a higher effective absorption correction than required by just using substrate optical constants, we could model the observed reduced enhancement at the substrate critical angle. This effective Vinyard factor may be written as

$$\tilde{V}_{eff}(k_{i\perp}, k_{f\perp}, v) = \left| \frac{2k_{f\perp}}{k_{f\perp} + \sqrt{k_{f\perp}^2 - k_c^2 + iv}} \right|^2 \tag{16}$$

The effective absorption factor $v$ is given as $\beta/\delta$ for a free surface with the X-ray optical constants for refraction $\delta$ and absorption $\beta$ of the substrate,[32] however, in our model we treat it as a fitting parameter.

**d. Scattering from Monolayers.** With the ingredients introduced above (see also Figure 2), we have a model to describe the scattering from partial monolayers up to a full monolayer:[14]

$$I_{ML}(q_\parallel, q_\perp) \propto \bar{F}(q)Z(q_\parallel)V_{eff}(q_\perp) \tag{17}$$

It is interesting to take a look at how these different contributions come together: the structure factor determines the positions of $q_\parallel$ at which scattering can take place. The intensity streaks perpendicular to the surface at these in-plane positions are the so-called scattering rods well-known from grazing-incidence diffraction.[32,35,36] For nanocrystal monolayers, the modulation of the rod intensity results from the nanocrystal form factor rather than scattering from single atoms or molecules. The intensity cutoff at the sample horizon and the dynamic enhancement of the scattering intensity at the critical angle are given by the Vinyard factor.

**e. Scattering from Multiple Layers.** There are two well-known stacking sequences of spherical objects: face-centered cubic (FCC) with (111) planes forming hexagonal layers, and hexagonal close-packed (HCP) with (001) basal planes of hexagonally ordered layers. The FCC and HCP lattices are closely related and only differ in their stacking sequences ABCABC... and ABABAB..., respectively. Both lattices yield the same space-filling. In colloidal crystals, random HCP (RHCP) stacking is also observed, in which the stacking fluctuates unpredictably between FCC and HCP.[37,38] We will show in the following that GISAXS intensities can provide information to distinguish the subtle differences between these structures, and how the hexagonal monolayers are stacked.

Starting from the monolayer structure factor, $Z_0(q_x)$, given in eq 6, a full structure factor for a 2D powder of multilayer stacks can be obtained. If the first monolayer (position A) is packed hexagonally, there are two possibilities to continue with the

second layer (positions B or C), since only three of the six available 3-fold coordinated sites can be occupied at a time by nanocrystals of the second monolayer (see Figure 1). Still, the scattering will remain the same for either position. At the start of the third monolayer, the nanocrystals can pack in either FCC (position sequence A B C A B C) or in HCP positions (position sequence A B A B A B). Such finite stacks of layers only yield the full 3D lattice symmetry after multiples of three layers (FCC) or two layers (HCP) are filled. Otherwise the films have only a partially filled bulk unit cell on top. Only at six layers do both FCC and HCP packed layers display diffraction corresponding to full unit cells simultaneously. As partially filled bulk unit cells may show some unusual scattering,[35,36] we will compare both stacking sequences up to this point.

For this task, it is the most efficient to introduce crystallographic coordinates. If the hexagonal lattice of the first layer (position A) is described in units of hexagonal lattice vectors,

$$a = (a, 0)$$
$$b = (a/2, -a\sqrt{3}/2) \tag{18}$$

the reference position A in the bottommost layer can by chosen as $(0,0,0)$. For ideal hard spheres, the second layer is at a height of

$$c = a\sqrt{8}/3 \tag{19}$$

above the first layer, defining the third lattice parameter $c$. Then layer B corresponds to $(1/3,2/3,1)$ with respect to these lattice vectors. For the third layer, there is either FCC packing associated with position C or $(2/3,1/3,2)$ or HCP packing with position A, now in the third layer or $(0,0,2)$.

The comparison between the FCC and HCP lattice positions for the first six layers is shown in Table 1. Note that we have constructed a nonstandard FCC unit cell that reflects the arrangement of particles at the substrate surface, the FCC(111) surface unit cell.[35,36]

**Table 1. Relative Positions of FCC and HCP-Stacked NC Layers within the Surface Unit Cell**

| layer | FCC | HCP |
|---|---|---|
| 1 | (0,0,0) | (0,0,0) |
| 2 | (1/3,2/3,1) | (1/3,2/3,1) |
| 3 | (2/3,1/3,2) | (0,0,2) |
| 4 | (0,0,3) | (1/3,2/3,3) |
| 5 | (1/3,2/3,4) | (0,0,4) |
| 6 | (2/3, 1/3,5) | (1/3,2/3,5) |

The scattering rods associated with a total of $N$ monolayers are then given by

$$S_N(h, k, l) = \sum_{n=0}^{N-1} \beta^n \exp[2\pi i(hx_n + ky_n + Lz_n)] \tag{20}$$

where $(x_n, y_n, z_n)$ are the relative positions of the layer atoms as given in Table 1, $(h,k)$ is the index of the in-plane reflection, and $L = cq_\perp/2\pi$ is the continuous relative wave vector component in the direction of the scattering rod. The occupation factor $\beta$ was included to account for partial occupancy of the second monolayer and successive layers.[39]

For performing the powder average around the surface normal, we have to take into account that the $(10L)$ rod and

the (01L) rod in FCC do not have the Bragg reflections at the same L, while their in-plane q-vectors are degenerate. Hence, in the 2D powder scattering, these rods appear to be superimposed, each with a multiplicity of 3 (see Figure 4). Similar
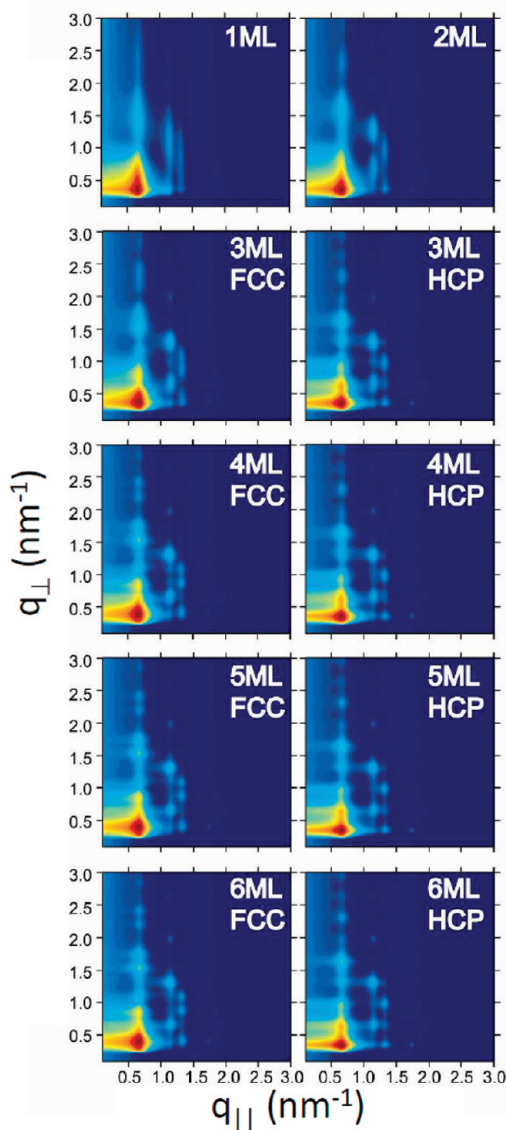


**Figure 4.** Evolution of the calculated scattering intensity for 1−6 layers. Starting at three layers, FCC and HCP stacking differ. Distinctive differences between scattering from FCC- and HCP-stacked layers appear clearly already at four monolayers. For FCC stacking, the appearance of scattering from six monolayers is already close to the bulk case.[6] Intensities are shown on a logarithmic scale.

considerations have to be made for all other FCC rods with $h \neq k$. In compact form, this behavior can be written as

$$S_N^{av}(q_{hk}, q_\perp) = \frac{m_{hk}}{2}\left\{S_N\left(h, k, \frac{cq_\perp}{2\pi}\right) + S_N\left(k, h, \frac{cq_\perp}{2\pi}\right)\right\}$$

(21)

which remains correct for the special case $h = k$, where $S_N(h,k,L)$ and $S_N(k,h,L)$ are identical. This extra complication does not occur for the HCP scattering rods which maintain the same multiplicity of 6 or 12 as the in-plane reflections $(h,k)$. The deeper reason for this difference is that, due to the packing,

FCC layers only have a 3-fold symmetry axis, while HCP layers maintain the 6-fold symmetry of the monolayer.

The full structure factor for a 2D powder of multilayer stacks is thus given as

$$Z_N(q_\parallel, q_\perp) = \sum_{hk} L(q_\parallel - q_{hk}, w_{hk})S_N^{av}(q_{hk}, q_\perp)$$

(22)

Finally the intensity distribution for a multilayer with a well-defined height of N layers can be written as

$$I_N(q_\parallel, q_\perp) \propto \bar{F}(q)Z_N(q_\parallel, q_\perp)V_{eff}(q_\perp)$$

(23)

The associated theoretical 2D scattering images for N perfect layers are shown in Figure 4. Scattering along certain rods such as (11L) is very similar; however, the rods with $h \neq k$ such as (10L) reveal the 3-fold or 2-fold stacking sequence characteristic for FCC and HCP, respectively.

**f. Imperfect Layering.** Deposition of multiple layers can result in finite grains of variable height. Hence, if the multilayer stacks have variable height N, the scattering signal can be obtained by averaging using a Poisson distribution of N with expectation value $\Lambda$, where we define $Z_0$ as 0 (no deposit) and $Z_1 = Z(q_\parallel)$ (monolayer):

$$\bar{Z}_{mult}(q_\parallel, q_\perp) = \sum_N \exp(-\Lambda)\frac{\Lambda^N}{N!}Z_N(q_\parallel, q_\perp)$$

(24)

The most general expression for the full multilayer scattering intensity is thus given by

$$\bar{I}_{mult}(q_\parallel, q_\perp) \propto \bar{F}(q)\bar{Z}_{mult}(q_\parallel, q_\perp)V_{eff}(q_\perp)$$

(25)

including the form factor $\bar{F}(q)$, scattering factor $\bar{Z}_{mult}(q_\parallel,q_\perp)$, and Vineyard factor $V(q_\perp)$.

**g. Monolayer Stacking.** In the considerations so far, we have focused on pure FCC and HCP lattices. However, the small energetic difference between FCC and HCP sites can lead to the formation of stacking faults, in particular under conditions of fast deposition kinetics. Thus, in colloidal systems with particle sizes about 10 to 100 times larger than nanocrystals, often RHCP stacking is found.[35] The characteristic RHCP streaks of the (10L) rods can be understood as superposition of the FCC and HCP reflections. In such a situation, the statistical modeling, even for only a few layers, can become quite elaborate, with the coexistence of pure FCC and HCP islands in addition to islands with stacking faults.

We observe that the full complexity actually starts with the formation of a fourth layer: As mentioned above, FCC and HCP stacking are not distinguishable with only two layers. More specifically, a mix of AB and AC stacked layers will not make a change in the incoherent uniaxial powder average. Similarly, there are no stacking faults in the three-layer system: the four possible stackings are either FCC (ABC and ACB) or HCP (ABA and ACA). Hence the three-layer system can be modeled as a mix of FCC and HCP islands in a straightforward extension of $I_{mult}$ (eq 25). We will leave it to the reader to investigate the statistics for four and more layers. Note that a statistical theory of RHCP for multiple layers has already been described by Loose et al.[35]

**h. Computational Methods.** The GISAXS model was prototyped using Mathcad 2000 Professional and then translated into Matlab 7.1. Computations were performed on standard PCs, and completed simulations took 2−3 min. Input parameters of the model include the 2D hexagonal lattice

constant $a$ (nm), inorganic nanocrystal core diameter $d$ (nm) and diameter distribution (% standard deviation), shape of the scatterer (spherical), interface absorption parameter ($v = 0.01$), incident angle of radiation ($\alpha_i = 0.25°$), grain size $D = 2\pi K/2\Gamma$, and static Debye–Waller factor $B$. The lattice structure was determined by indexing the scattering peaks from the experimental monolayer GISAXS patterns, and the average grain size was estimated by Scherrer analysis of the peak breadth.[33] Using this information, the Debye–Waller factor was determined by best fitting the model to the experimental GISAXS data.

### ■ RESULTS AND DISCUSSION

SEM images of the monolayer, bilayer, and trilayer LB deposited films are shown in Figure 5. The monolayer and
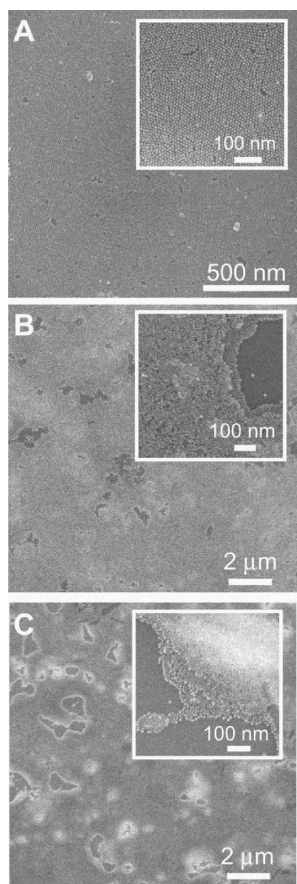


**Figure 5.** SEM images after (A) one, (B) two, (C) three LB deposition cycles of FePt nanocrystal monolayers onto a Si substrate. The monolayer and the bilayer appear as relatively smooth, while the nominal trilayer displays disorder.

the bilayer show densely packed hexagonal layers, with a higher amount of defects, especially holes, in the bilayer. The nominal trilayer features even more, and larger size, holes in the film. It appears that small patches of nanocrystals pull away from the film during the third deposition step. As the film thickness increases, the adhesion to the underlying substrate becomes weaker, which leads to more fragile films with more defects and reduced long-range ordering of nanocrystals. The resulting hill-and-valley morphology is reminiscent of 3D growth.

GISAXS data were collected from monolayer, bilayer, and trilayer LB deposited films. As the first step in the analysis, the

horizontal and vertical line cuts (see Figure 6) of the 2D GISAXS images (Figure 7A) were analyzed and fitted using the model described above; this specifies the lattice constants, grain size, and in-plane degree of disorder. The horizontal line cuts (see Figure 6A) were chosen along the Yoneda band, i.e., the bright strip of intensity close to the sample horizon in which the scattering is enhanced by the Vinyard effect. For better statistics, we averaged over 10 pixels vertically. Next, the intensity along the observed rods were fitted, as shown in Figure 6B−E. These simultaneous fits determine the layering structure as well as the particle size distribution in the form factor. In addition, the effective X-ray absorption at the interface was adjusted using the vertical line cuts. Finally, the full 2D intensity distributions were calculated and compared with experimental images (Figure 7).

The three films were found to have the same lateral lattice constant of 11.0 nm and quite similar lateral grain sizes of about 60 nm, 55 nm, and 40 nm for the nominally one, two, and three layer films, respectively. The monolayer shows nice in-plane ordering with scattering up to the fourth order, i.e., the (21) hexagonal peak can be clearly discerned. The bilayer sample displays noticeably increased overall disorder, as fewer scattering rods were detected. The difference of the scattering strength at high $q_{\parallel}$ is accounted for by differing degrees of static disorder, as given by the Debye–Waller factors of 1.15 nm, 1.30 nm, and 2.15 nm for the three layers, respectively.

The rods for the monolayer and bilayer could be modeled quite well. In particular, the narrowing of the maxima along the (10 L) rod due to the formation of a second layer in registry with the first one was reproduced nicely for the bilayer sample. The coverage parameter $\beta$ for the second layer was found to be close to 1, consistent with the SEM image. The observed lattice registry between the two layers indicates that there must be significant interaction between the base monolayer and the top layer during the LB deposition process.

The trilayer film, on the other hand, displayed significant disorder. All of the finer structure that an ideal trilayer should show in scattering was lost, indicating that the nominal trilayer film is more characteristic of a mixture of small grains with varying layer numbers. SEM confirmed that this was indeed the arrangement of the nanocrystals, as there is significant irregularity in the film, especially due to the presence of many holes, which seems to lead to a significant amount of disorder in the superlattice structure at the hole edges. The GISAXS scattering rods from the nominal trilayer film more closely resembled the bilayer scattering than the scattering expected from a trilayer structure. In addition to the weak and broad scattering signals, the GISAXS intensity also showed orientational disorder, which produces the arc-like (rather than streak-like) appearance of the diffraction features. This type of orientational disorder, also termed mosaicity, is presently not accounted for in our model.

Nanocrystal monolayers absorb readily on various substrates with hexagonal symmetry.[5] Strong adsorbate−substrate interaction, mainly due to the van-der-Waals interaction between substrate surface and nanocrystal cores, leads to monolayer stability. The smoothness of the substrate is also important: oriented nanocrystal layers do not form on rough surfaces, but rather randomly oriented supracrystals are formed.[6] From the SEM results, we see that the second nanocrystal layer still absorbs reasonably well and with good order, orientation, and registry, to an underlying nanocrystal monolayer.
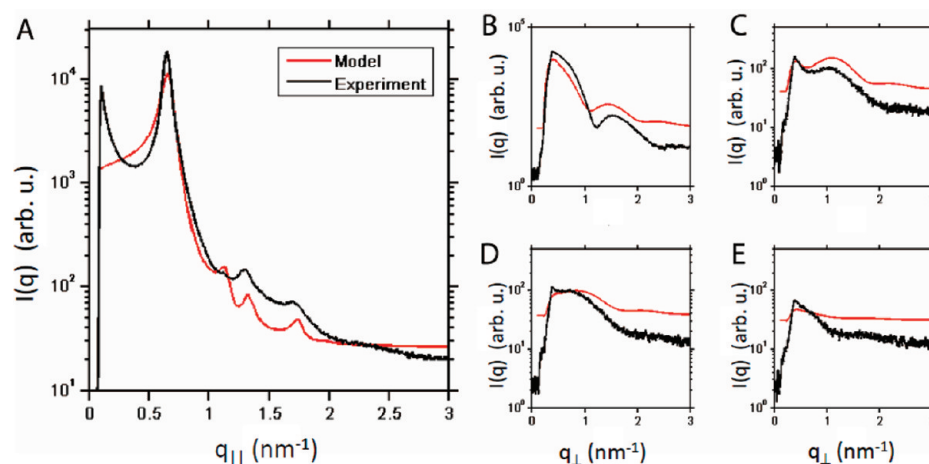
**Figure 6.** Line slice averages of the scattering from a single nanocrystal monolayer along the (A) Yoneda band, (B) (10) Bragg rod, (C) (11) Bragg rod, (D) (20) Bragg rod, and (E) (21) Bragg rod (black lines). A simultaneous fit of all five experimental curves is shown (red lines) in addition. The fits capture the essential features such as peak positions and line widths.

For a rough estimate of the relevant interaction energies, we used the Hamaker constants of gold and silver in hexane of about $A = 1.5$ eV[40] or $A = 60$ $k_B T$ (at room temperature) to model the FePt layers with a nanoparticle radius of $R = 3.5$ nm and a 2 nm thick ligand shell. The ligand shell serves as a dielectric spacer between nanocrystals with a much lower Hamaker constant of 0.1 eV. Applying the Hamaker formulas for a particle close to a dielectric wall and for two particles of equal size,[41] we found that the first layer is bound with about 4 $k_B T$, while the binding energy between two nanocrystals corresponds to only about 0.2 $k_B T$. If a second layer of particles attaches to the first layer of particles in a 3-fold coordinated position, this increases the adsorbate–adsorbate interaction to 0.6 $k_B T$. Hence, the adhesion of the second layer of nanocrystals is much weaker than the first layer of nanocrystals contacting the underlying support.

Starting at the third layer, we observed that the adsorption is far less organized. For pure adsorbate–adsorbate interactions between nanocrystals, step edges provide the highest degree of coordination and become energetically favored adsorption sites. Moreover, cluster formation becomes favorable for the same reason, while there is not a perfectly smooth reference layer any more, as was the first layer to the second layer particles. At this point, deposition leads to rougher films even though the LB technique is designed to promote the deposition of a single close-packed layer per cycle. It is possible that due to weaker interactions the adsorption kinetics is slower and that the pulling rate and the surface pressure in the LB trough would need to be adjusted to this situation. In addition, the weaker adsorbed layer seems to be more prone to defect formation and loss of orientational coherence.

There may also be an analogy with atomic growth, where three growth modes prevail: (i) Frank–van der Merve proceeds layer by layer; this was the growth mode we were aiming for. (ii) Stranski–Krastanov (SK) growth starts layer-by-layer, but at a critical thickness 3D islands are formed. (iii) Vollmer–Weber growth forms 3D islands of deposits right from the start.[42] The transition from bilayer to trilayer is reminiscent of SK growth in epitaxial growth. In SK growth, the morphological transformation at the critical film thickness is strain-driven: In atomic epitaxial growth, strain is typically caused by misfit with the substrate lattice. The LB deposition of the second and third layers were carried out at a lateral pressure of 30 mN/m to ensure compaction of the monolayer, which may have been too high, leading to significant strain in the deposited monolayer. Recent studies of nanoparticle Langmuir layers at the air–water interface[43,44] have shown that nanocrystal monolayers can already collapse at surface pressures in the range of 10–20 mN/m, and bilayers or multilayers are formed. Relaxation of the strain upon monolayer transfer may have led to a 3D morphology as the third layer was deposited. An additional factor favoring this transformation is that the van der Waals interaction between adjacent layers is smaller than between the first layer and the substrate. So while the first layer is stabilized by the substrate, subsequent layers are more susceptible to this instability.

Recently, Chitu and co-workers succeeded in preparing a six-layer film by LB deposition on a chemically modified substrate.[45] While X-ray reflectivity measurements clearly show the layering in the film, GISAXS images resembled rather monolayer or bilayer scattering. Apparently, the registry between adjacent layers was mostly lost. This work demonstrated that further progress can be achieved with LB deposition past the trilayer. The poor registry of layers points to another issue of the method: The new layer is deposited as a whole layer rather than particle by particle. As is the case for a monolayer at the air–water interface,[10] such a layer consists of randomly oriented patches of hexagonally ordered particles separated by grain boundaries. When such a film is deposited on a previous one, the patches are usually not lined up, and kinetic hindrances may prevent them from doing so. It would be interesting to study whether a low deposition speed could overcome these hindrances or whether solvent annealing of the deposits[6] can improve the registry.

The third adsorbed layer plays a crucial role in superlattice formation: at this point the system has to decide whether to form FCC or HCP stacking or, when energy differences are too small, RHCP. The latter stacking is commonly observed in colloidal crystals, where the typical particle dimension (100 nm to several micrometers) is much larger than for nanocrystals (2–10 nm). In ref 38, the formation of well-ordered and well-oriented two-layer and a seven-layer colloidal crystal is reported using a convective self-assembly technique. The seven-layer film already showed pronounced RHCP packing.

In contrast to both our LB films and colloidal deposits, dropcast nanocrystal solutions under slow drying conditions
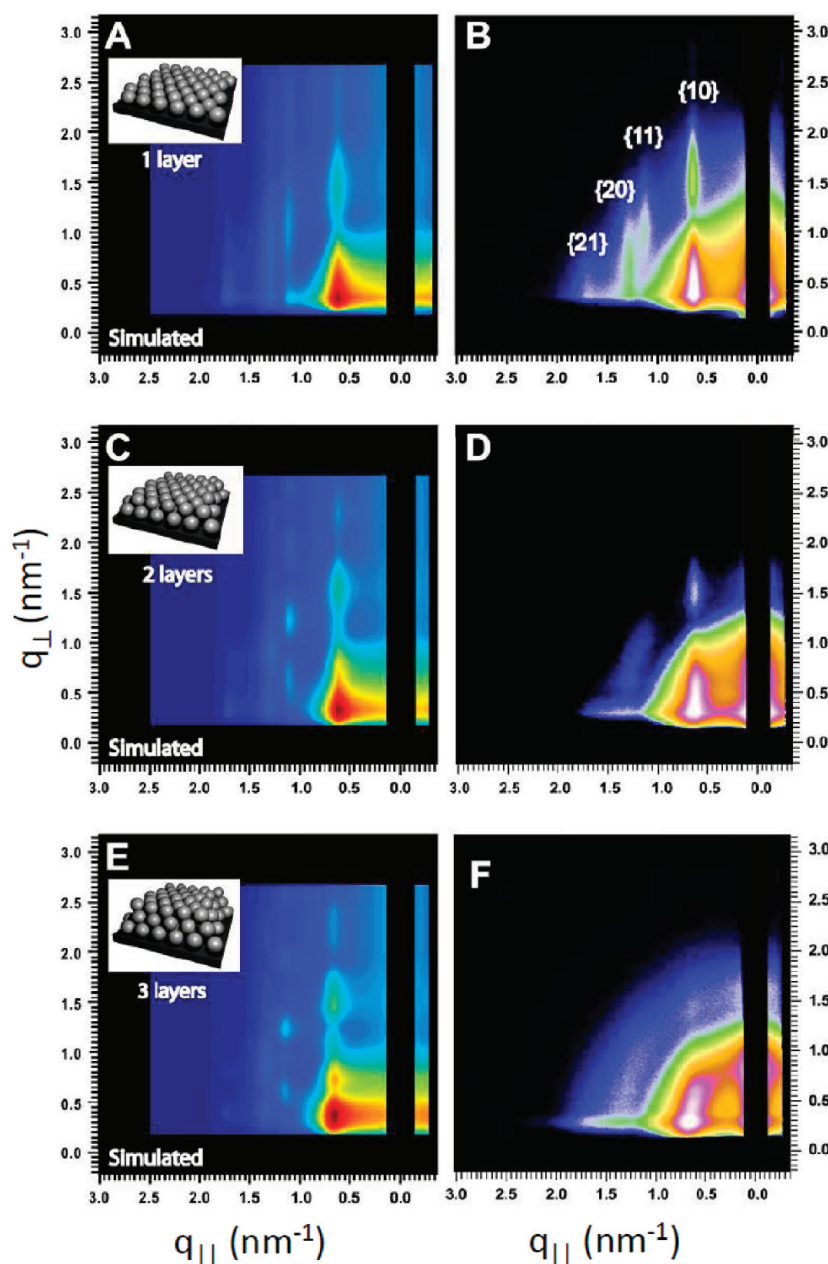
**Figure 7.** Comparison of the model to experimental data for (A,B) one, (C,D) two, and (E,F) three FCC stacked FePt nanocrystal monolayers. The monolayer and bilayer scattering is reproduced quite well, particularly the narrowing of the scattering features along the {10 L} scattering rod. The nominal trilayer shows more disorder and effectively resembles more the bilayer (C,D) than the calculated trilayer (E). Intensities are shown on a logarithmic scale.

form supracrystals of micrometer size featuring perfect FCC stacking and alignment of the (111) faces parallel to the substrate.[6] A similar result was obtained with convective self-assembly.[16] One may argue that such supracrystals spontaneously nucleate and grow in a 3D mode in the solution phase; however, this contradicts the perfect surface alignment of the (111) superlattice facets recently observed.[6,16,19] It is in fact possible for supracrystals to nucleate in the bulk of the solution film under fast drying conditions and associated kinetic hindrance, but in this case the resulting deposits lose their orientation with respect to the substrate and display only powder rings.[6] Hence a 3D crystallization in the bulk of the solution cannot explain the emergence of oriented supracrystals via drop casting.

Combining the results from LB deposition and slow drop casting, the nanocrystal growth mode must have both 2D and 3D aspects, highlighting the importance of what happens at the third layer. At this point we do not have a definite answer to this intriguing crystallization problem, however, our paper provides the tools to analyze the formation of the third and consecutive layers as well as the stacking in detail. The challenge remains whether nanocrystal films with a finite number of well stacked layers can be prepared past the bilayer. More careful LB deposition, convective self-assembly, or hot doctor blading in combination with in situ GISAXS may be attempted to probe this critical step further.

## ■ CONCLUSION

For the analysis of the stacking properties of hexagonal NC layers, we modeled GISAXS intensities for up to six layers of nanoparticles using the quasi-kinematic approximation. Our method should be applicable to other hexagonal layers formed by nanoscale spherical objects, such as micelles.[46] Our simplified model can be readily adapted to other nanoscale lattices. The main asset of the quasi-kinematic description is that classic SAXS concepts such as form factor and structure factor can be easily identified in the scattering images, and the scattering theory remains transparent.

We prepared multiple layers of spherical FePt nanocrystals on solid substrates using the LB technique. The nominal monolayer, bilayer, and trilayer were characterized with SEM and GISAXS. While mono- and bilayer appeared to be well-ordered, the nominal trilayer showed a substantial amount of disorder, both in electron microscopy and scattering. Comparing these results to the large, micrometer-sized nanocrystal supracrystals obtained in slow drop casting onto smooth substrates, we identified an intriguing crystallization problem at the level of the third layer, that sets nanocrystals with their perfect FCC superlattices apart from their larger cousins, the stacking-fault-prone colloidal crystals.

## ■ AUTHOR INFORMATION

**Corresponding Author**
*E-mail: dms79@cornell.edu.

**Notes**
The authors declare no competing financial interest.

## ■ ACKNOWLEDGMENTS

## ■ REFERENCES

(1) Collier, C. P.; Vossmeyer, T.; Heath, J. R. *Annu. Rev. Phys. Chem.* **1998**, *49*, 371−404.
(2) Wang, Z. L. *Adv. Mater.* **1998**, *10*, 13−30.
(3) Korgel, B. A.; Fullam, S.; Connolly, S.; Fitzmaurice, D. *J. Phys. Chem. B* **1998**, *102*, 8379−8388.
(4) Whetten, R. L.; Shafigullin, M. N.; Khoury, J. T.; Schaaff, T. G.; Vezmar, I.; Alvarez, M. M.; Wilkinson, A. *Acc. Chem. Res.* **1999**, *32*, 397−406.
(5) Korgel, B. A.; Fitzmaurice, D. *Phys. Rev. Lett.* **1998**, *80*, 3531−3534.
(6) Hanrath, T.; Choi, J. J.; Smilgies, D.-M. *ACS Nano* **2009**, *3*, 2975−2988.
(7) James, R.; Heath, J. R.; Knobler, C. M.; Leff, D. V. *J. Phys. Chem. B* **1997**, *101*, 189−197.
(8) Brust, M.; Stuhr-Hansen, N.; Nørgaard, K.; Christensen, J. B.; Nielsen, L. K.; Bjørnholm, T. *Nano Lett.* **2001**, *1*, 189−191.
(9) Chen, S. *Langmuir* **2001**, *17*, 2878−2884.
(10) Schultz, D. G.; Lin, X.-M.; Li, D.; Gebhardt, J.; Meron, M.; Viccaro, P. J.; Lin, B. *J. Phys. Chem. B* **2006**, *110*, 24522−24529.
(11) Tao, A. R.; Huang, J.; Yang, P. *Acc. Chem. Res.* **2008**, *41*, 1662−1673.
(12) Aleksandrovic, V.; Greshnykh, D.; Randjelovic, I.; Frömsdorf, A.; Kornowski, A.; Roth, S. V.; Klinke, C.; Weller, H. *ACS Nano* **2008**, *2*, 1123−1130.
(13) Patel, R. N.; Heitsch, A. T.; Hyun, C.; Smilgies, D.-M.; De Lozanne, A.; Loo, Y.-L.; Korgel, B. A. *ACS Appl. Mater. Interfaces* **2009**, *1*, 1339−1346.
(14) Heitsch, A. T.; Patel, R. N.; Goodfellow, B. W.; Smilgies, D.-M.; Korgel, B. A. *J. Phys. Chem. C* **2010**, *114*, 14427−14432.
(15) Siffalovic, P.; Chitu, L.; Majkova, E.; Vegso, K.; Jergel, M.; Luby, S.; Capek, I.; Satka, A.; Maier, G.; Keckes, J.; et al. *Langmuir* **2010**, *26*, 5451−5455.
(16) Dunphy, D.; Fan, H.; Li, X.; Wang, J.; Brinker, C. J. *Langmuir* **2008**, *24*, 10575−10578.
(17) Shevchenko, E. V.; Talapin, D. V.; Murray, C. B.; O'Brien, S. *J. Am. Chem. Soc.* **2006**, *128*, 3620−3637.
(18) Shevchenko, E. V.; Talapin, D. V.; Kotov, N. A.; O'Brien, S.; Murray, C. B. *Nature* **2006**, *439*, 55−59.
(19) Smith, D. K.; Goodfellow, B.; Smilgies, D. M.; Korgel, B. A. *J. Am. Chem. Soc.* **2009**, *131*, 3281−3290.
(20) Bodnarchuk, M. I.; Kovalenko, M. V.; Pichler, S.; Fritz-Popovski, G.; Hesser, G.; Heiss, W. *ACS Nano* **2010**, *4*, 423−431.
(21) Smilgies, D.-M.; Busch, P.; Posselt, D.; Papadakis, C. M. *Synchrotron Radiation News* **2002**, *15* (5), 35−42.
(22) Smilgies, D.-M. (2003). On-line GISAXS tutorial. http://staff.chess.cornell.edu/~smilgies/gisaxs/GISAXS.php.
(23) Saunders, A. E.; Ghezelbash, A.; Smilgies, D.-M.; Sigman, M. B., Jr.; Korgel, B. A. *Nano Lett.* **2006**, *6*, 2959−2963.
(24) Talapin, D. V.; Lee, J.-S.; Kovalenko, M, V.; Shevchenko, E. V. *Chem. Rev.* **2010**, *110*, 389−458.
(25) Chen, M.; Liu, J. P.; Sun, S. H. *J. Am. Chem. Soc.* **2004**, *126*, 8394−8395.
(26) Sinha, S. K.; Sirota, E. B.; Garoff, S.; Stanley, H. B *Phys. Rev. B* **1988**, *38*, 2297−2311.
(27) Lazzari, R. *J. Appl. Crystallogr.* **2002**, *35*, 406−421.
(28) Lazzari, R.; Renaud, G.; Jupille, J.; Leroy, F. *Phys. Rev. B* **2007**, *76*, 125412.
(29) Naudon, A. In *Modern Aspects of Small-Angle Scattering*; Brumberger, H., Ed.; Kluwer: Dordrecht, The Netherlands, 1995; pp 181−202
(30) Förster, S.; Timmann, A.; Konrad, M.; Schellbach, C.; Meyer, A.; Funari, S. S.; Mulvaney, P.; Knott, R. *J. Phys. Chem. B* **2005**, *109*, 1347−1360.
(31) Vineyard, G. H. *Phys. Rev. B* **1982**, *26*, 4146−4159.
(32) Als-Nielsen, J.; McMorrow, D. F. *Elements of Modern X-ray Physics*; John Wiley & Sons: New York, 2001.
(33) Smilgies, D.-M. *J. Appl. Crystallogr.* **2009**, *42*, 1030−1034.
(34) Babonneau, D. *J. Appl. Crystallogr.* **2010**, *43*, 929−926.
(35) Loose, W.; Ackerson, B. *J. Chem. Phys.* **1994**, *101*, 7211−7220.
(36) Huber, P.; Bunk, O.; Pietsch, U.; Textor, M.; Geue, T. *J. Phys. Chem B* **2010**, *114*, 12473−12479.
(37) Feidenhans'l, R. *Surf. Sci. Rep.* **1989**, *10*, 105−188.
(38) Robinson, I. K.; Tweet, D. *Rep. Prog. Phys.* **1992**, *55*, 599−651.
(39) Robinson, I. K. *Phys. Rev. B* **1986**, *33*, 3830−3836.
(40) Sigman, M. B., Jr.; Saunders, A. E.; Korgel, B. A. *Langmuir* **2004**, *20*, 978−983.
(41) Hamaker, H. C. *Physica* **1937**, *4*, 1058−1072.
(42) Venables, J. A.; Spiller, G. D. T.; Hanbücken, M. *Rep. Prog. Phys.* **1984**, *47*, 399−459.
(43) Fukuto, M.; Heilmann, R. K.; Pershan, P. S.; Badia, A.; R. Bruce Lennox, R. B. *J. Chem. Phys.* **2004**, *120*, 3446−3459.
(44) Schultz, D. G.; Lin, X.-M.; Li, D.; Gebhardt, J.; Meron, M.; Viccaro, P. J.; Lin, B. *J. Phys. Chem. B* **2006**, *110*, 24522−24529.
(45) Chitu, L.; Siffalovic, P.; Majkova, E.; Jergel, M.; Vegso, K.; Luby, S.; Capek, I.; Satka, A.; Perlich, J.; Timmann, A.; et al. *Meas. Sci. Rev.* **2010**, *10*, 162−165.
(46) Wolff, M.; Scholz, U.; Hock, R.; Magerl, A.; Leiner, V.; Zabel, H. *Phys. Rev. Lett.* **2004**, *92*, 255501.